The Astrophysical Journal Letters, 944:L48 (14pp), 2023 February 20 https://doi.org/10.3847/2041-8213/acb6f4

Radiation Transport Two-temperature GRMHD Simulations of Warped Accretion Disks

M. T. P. Liska[1], N. Kaaz[2], G. Musoke[3], A. Tchekhovskoy[2], and O. Porth[3]
[1] Institute for Theory and Computation, Harvard University, 60 Garden Street, Cambridge, MA, 02138, USA; matthew.liska@cfa.harvard.edu
[2] Center for Interdisciplinary Exploration & Research in Astrophysics (CIERA), Physics & Astronomy, Northwestern University, Evanston, IL, 60202, USA
[3] Anton Pannekoek Institute for Astronomy, University of Amsterdam, Science Park 904, 1098 XH Amsterdam, The Netherlands
Received 2022 October 22; revised 2022 December 20; accepted 2022 December 20; published 2023 February 22

Abstract

In many black hole (BH) systems, the accretion disk is expected to be misaligned with respect to the BH spin axis. If the scale height of the disk is much smaller than the misalignment angle, the spin of the BH can tear the disk into multiple, independently precessing "sub-disks." This is most likely to happen during outbursts in black hole X-Ray binaries (BHXRBs) and in active galactic nuclei (AGNs) accreting above a few percent of the Eddington limit, because the disk becomes razor-thin. Disk tearing has the potential to explain variability phenomena including quasi-periodic oscillations in BHXRBs and changing-look phenomena in AGNs. Here, we present the first radiative two-temperature general relativistic magnetohydrodynamic (GRMHD) simulation of a strongly tilted (65°) accretion disk around an $M_{\rm BH} = 10\,M_\odot$ BH, which tears and precesses. This leads to luminosity swings between a few percent and 50% of the Eddington limit on sub-viscous timescales. Surprisingly, even where the disk is radiation-pressure-dominated, the accretion disk is thermally stable over $t \gtrsim 14{,}000\,r_g/c$. This suggests warps play an important role in stabilizing the disk against thermal collapse. The disk forms two nozzle shocks perpendicular to the line of nodes where the scale height of the disk decreases tenfold and the electron temperature reaches $T_e \sim 10^8$–10^9 K. In addition, optically thin gas crossing the tear between the inner and outer disk gets heated to $T_e \sim 10^8$ K. This suggests that warped disks may emit a Comptonized spectrum that deviates substantially from idealized models.

Unified Astronomy Thesaurus concepts: Galaxy accretion disks (562); BH physics (159); Magnetohydrodynamical simulations (1966); Stellar accretion disks (1579)

1. Introduction

Accretion disks in black hole (BH) X-ray binaries (BHXRBs) and active galactic nuclei (AGNs) are typically described by axisymmetric, time-independent models. A key factor that determines the most suitable model is the accretion rate with respect to the Eddington limit. At the Eddington limit, radiation pressure rivals gravity and plays a dynamically important role. The most well-known models are the geometrically thin standard accretion disk model (Shakura & Sunyaev 1973), which describes sources accreting at an appreciable fraction of their Eddington limit ($L \gtrsim 0.01$–$0.1\,L_{\rm Edd}$), and the geometrically thick advection dominated accretion flow model (Narayan & Yi 1994; Narayan et al. 2003), which describes highly sub-Eddington sources ($L \lesssim 0.01\,L_{\rm Edd}$). Slim disk models, in which the advection of trapped photons dominates, work well near and above the Eddington limit (e.g., Abramowicz et al. 1978). While these models can provide a reasonable description of the multi-wavelength emission, they—by construction—do not address the variability of their light curves and spectra. Such variability can encode important information about the structure of the accretion disk and corona (e.g., Uttley et al. 2014; Kara et al. 2019).

For example, recent observational evidence indicates that accretion disks in changing-look AGNs can undergo drastic changes in luminosity and spectral shape over the course of less than a year (e.g., MacLeod et al. 2016; Yang et al. 2018) or during quasi-periodic eruptions (QPEs) over the course of hours (e.g., Yang et al. 2018). In these AGNs, the luminosity can change by up to two orders of magnitude, while the spectrum significantly hardens or softens. This suggest a dramatic change in the accretion flow on timescales which are too short to be explained by the viscous timescales inferred from the Maxwell stresses created by magnetorotational instability (MRI; Balbus & Hawley 1991, 1998) induced turbulence (e.g., Lawrence 2018; Dexter & Begelman 2019). Various physical mechanisms were proposed to reconcile theory with observations, including instabilities in the accretion disk (Sniegowska et al. 2020), magnetically elevated accretion disks (Begelman & Pringle 2007), reprocessing of point-source radiation by the outer accretion disk (e.g., Clavel et al. 1992), disk tearing (Raj & Nixon 2021), and an orbiting compact object (e.g., King 2020; Arcodia et al. 2021).

Similar to their changing-look AGN counterparts, the power spectra of BHXRBs display a wide range of mysterious features ranging from broad-spectrum variability to narrow spectral peaks known as quasi-periodic oscillations (QPOs). Such features can encode unique information about the structure and dynamics of the accretion disk in addition to the spin and mass of the BH. QPOs are typically divided into low- and high-frequency QPOs, which can sometimes be observed together (e.g., Ingram & Motta 2019). Various physical mechanisms have been proposed to explain QPOs. These include geometric effects such as precession of a misaligned disk around the BH spin axis (e.g., Stella & Vietri 1998; Ingram & Done 2009) and intrinsic effects such as parametric resonances (e.g., Kluzniak & Abramowicz 2002; Rezzolla et al. 2003; Abramowicz & Kluźniak 2004) and discoseismic modes (e.g., Kato 2004; Dewberry et al. 2020a, 2020b). All of these models make

simplifying assumptions about the underlying physics. Most significantly, they typically do not include magnetized turbulence (though see Dewberry et al. 2020b; Wagoner & Tandon 2021), which can potentially dampen oscillatory modes. Thus, general relativistic magnetohydrodynamic (GRMHD) simulations, which can simulate accretion from first principles, are very attractive for addressing the origin of QPOs.

Interestingly, numerous GRMHD simulations have demonstrated that a misaligned disk can precess (e.g., Fragile & Anninos 2005; Fragile et al. 2007; Teixeira et al. 2014; Liska et al. 2018, 2019a; White et al. 2019). However, this only happens when the disk is unrealistically small and, in fact, Liska et al. (2018) demonstrated that the precession period of more realistically sized disks ($r \gtrsim$ a few hundred r_g) becomes too long to explain any observed QPOs. This problem can be solved if a smaller precessing disk tears of from a larger non-precessing disk due to the differential frame dragging (Lense & Thirring 1918) of spacetime by a spinning BH. This process, called disk tearing, was observed in various smoothed particle hydrodynamics (SPH) simulations (e.g., Nixon et al. 2012a, 2012b; Nealon et al. 2015; Raj et al. 2021) and recently confirmed by GRMHD simulations (Liska et al. 2021, 2022b). Disk tearing, interstingly, also leads to a rapid burst of accretion, possibly explaining the large luminosities and spectral swings observed in accreting BHs (e.g., Nixon & Salvesen 2013; Raj & Nixon 2021).

Musoke et al. (2023) recently addressed the origin of both low- and high-frequency QPOs using GRMHD simulations where a 65° misaligned accretion disk tore apart. Based on these simulations, Musoke et al. (2023) argued that low-frequency and high-frequency QPOs can be explained by disk tearing. In their model, a disk tears off at a near-constant radius ($r \sim 10^1\, r_g$) and precesses for $\lesssim$10 periods before falling into the BH. While precessing at $\nu = 2.5$ Hz (for $M_{\rm BH} = 10\, M_\odot$), the disk emits a periodically modulated light curve. Musoke et al. (2023) also found a prominent radial epicyclic oscillations at $\nu \sim 56$ Hz in the inner disk, which they argue can potentially explain some high-frequency QPOs. The geometric origin of low-frequency QPOs is supported by recent observations, which suggest that the iron line centroid frequency moves from blueshifted to redshifted with the same phase as the low-frequency QPO (Ingram & van der Klis 2014; Ingram et al. 2016). On the other hand, observations have been able to constrain neither an intrinsic nor geometric origin of the much rarer high-frequency QPOs (e.g., Ingram & Motta 2019).

Thus, the results of Musoke et al. (2023) suggest that disk tearing is a very promising mechanism to explain the multiwavelength variability in many accreting BHs. However, all GRMHD simulations that found tearing (Liska et al. 2021, 2022b) have relied on a cooling function (Noble et al. 2009) to set the temperature and scale height of the disk artificially. In reality, the temperature of the disk is determined by complex physics involving viscous heating, radiative cooling, and the advection of energy. Such physics can modify the radial and vertical structure of the disk, such as its scale height and vertical temperature profile. This makes it extremely challenging to benchmark such GRMHD models against multiwavelength observations because they might not capture the important physics that sets the disk's thermodynamic state. For example, in radiation-pressure-supported disks imbalance between the local dissipation rate and cooling rate can lead to thermal and viscous instabilities that are not captured by a cooling function (e.g., Lightman & Eardley 1974; Shakura & Sunyaev 1976; Sądowski 2016; Jiang et al. 2019; Liska et al. 2022a). In addition, when the inner disk precesses, it will beam its radiation field periodically toward the outer disk. This radiation field will scatter off the outer disk, and the radiation back-reaction force can cause additional warping and dissipation (e.g., Pringle 1997; Wijers & Pringle 1999).

Here, we present the first radiation transport two-temperature GRMHD simulation of an accretion disk tilted by 65° relative to a rapidly spinning $M_{\rm BH} = 10\, M_\odot$ BH with a dimensionless spin of $a = 0.9375$ accreting at 35% the Eddington luminosity. We show that the disk undergoes tearing. The accretion disk does not contain any large-scale vertical magnetic flux to begin with and does not launch a jet; this makes the simulation applicable to the soft(-intermediate) states of BHXRBs (see Fender et al. 2004). In Sections 2 and 3 we describe the numerical setup and initial conditions, before presenting and discussing our results in Sections 4 and 5, and concluding in Section 6.

2. Numerical Setup

In this work we utilize the radiative version of our GPU accelerated GRMHD code H-AMR (Liska et al. 2018, 2022b). H-AMR evolves the ideal GRMHD equations and radiation transfer equations in addition to the electron and ion entropies. We use a (modified) spherical grid in Kerr–Schild foliation with coordinates r, θ, and ϕ. Spatial reconstruction of primitive variables is performed using a 1D piecewise parabolic method (PPM), which guarantees second order convergence in three dimensions. Magnetic fields are evolved on a staggered grid as described in Gardiner & Stone (2005) and White et al. (2016). Inversion of conserved to primitive variables is performed using a 2D Newton–Raphson routine (Noble et al. 2006) or Aitken acceleration scheme (Newman & Hamlin 2014) for the energy equation and a 1D Newton–Raphson routine for the entropy equation. The energy-based inversion is attempted first, and, if it fails, the entropy-based inversion is used as a backup. This dual energy formulation is now standard in many GRMHD codes (Porth et al. 2019).

The radiative transfer equations are closed with a two-moment M1 closure (Levermore 1984) whose specific implementation is described in Sądowski et al. (2013) and McKinney et al. (2013). We additionally evolve (see, e.g., Noble et al. 2009; Ressler et al. 2015) the electron and ion entropy tracers ($\kappa_{e,i} = p_{e,i}/\rho^{\gamma_{e,i}}$) and include Coulomb collisions (Stepney 1983). We use adiabatic indices of $\gamma_e = \gamma_i = 5/3$ for the electrons and ions, respectively, and $\gamma = 5/3$ for the gas. This is appropriate for the ion and electron temperatures in the accretion disk. For a typical "peak" temperature of $T_e \sim 10^9$ K and $T_i \sim 10^{10}$ K we find that $\gamma_e \sim 1.57$, $\gamma_i \sim 1.66$, and $\gamma_g \sim 1.66$. We use a reconnection heating model (Rowan et al. 2017) to distribute the dissipative heating between ions and electrons. This leads to roughly 20%–40% of the dissipation going into the electrons with the remainder heating the ions.

We include Planck-averaged bound–free, free–free, and cyclo-synchrotron absorption ($\kappa_{\rm abs}$), emission ($\kappa_{\rm em}$), and electron scattering ($\kappa_{\rm es}$) opacities as given in McKinney et al. (2017) for solar abundances, where $X = 0.7$, $Y = 0.28$, and $Z = 0.02$. In addition, we account for Comptonization through a local blackbody approximation (Sądowski & Narayan 2015).

This works reasonably well when the emission, absorption, and scattering are localized, but becomes inaccurate when the radiation field is anisotropic and/or the energy spectrum deviates from a blackbody. Namely, the radiation temperature used to calculate the absorption opacity is approximated as a blackbody with $T_r = (\hat{E}_{\rm rad}/a)^{0.25}$, with $\hat{E}_{\rm rad}$ the fluid frame radiation energy density and a the radiation density constant. If the radiation deviates from a blackbody this approximation can severely under- or overestimate the radiation temperature. We assume that only electrons can absorb and emit radiation and set the ion opacity to $\kappa_i = 0$. This is a reasonable approximation in the accretion disk where bound–free processes, which involve energy exchange between ions/electrons/radiation, only become important when the density is high enough for Coulomb collisions to equilibrate the ion and electron temperatures. The limitations of the M1 closure relevant to our work are further addressed in Section 5.

To resolve the accretion disk in our radiative GRMHD models we use a base grid resolution of $N_r \times N_\theta \times N_\phi = 840 \times 432 \times 288$. We then use beyond $r \gtrsim 4\,r_g$ up to three layers of adaptive mesh refinement (AMR) to increase this resolution progressively in the disk from the base resolution at $r \sim 4\,r_g$ to $N_r \times N_\theta \times N_\phi = 6720 \times 2304 \times 4096$ at $r \sim 10\,r_g$. (In addition, we use static mesh refinement; Liska et al. 2022b; to reduce the ϕ-resolution to $N_\phi = 16$ at the polar axis.) This is exactly half of the resolution used in Liska et al. (2022b) and Musoke et al. (2023). We place the radial boundaries at $R_{\rm in} = 1.13\,r_g \approx 0.84\,r_{\rm H}$ and $R_{\rm out} = 10^5\,r_g$, which ensures that both boundaries are causally disconnected from the flow; here $r_{\rm H} = 1 + (1 - a^2)^{1/2} r_g$ is the event horizon radius. The local adaptive time-stepping routine in H-AMR increases the timestep of each mesh block independent of the refinement level in factors of two (up to a factor of 16) based on the local Courant condition (Courant et al. 1928). This increases the effective speed of the simulations severalfold while reducing the numerical noise (Chatterjee et al. 2019).

Since ideal GRMHD is unable to describe the physical processes responsible for injecting gas in the jet funnel (such as pair creation) we use density floors in the drift frame (Ressler et al. 2017) to ensure that $\rho c^2 \geqslant p_{\rm mag}/12.5$. However, due to the absence of any poloidal magnetic flux, no jets are launched in this work and thus the corresponding density floors are never activated. Instead, the ambient medium is floored at a density of $\rho = 10^{-7} \times r^{-2}$ and an internal energy of $u_{\rm tot} = 10^{-9} \times r^{-2.5}$, where $u_{\rm tot} = u_{\rm gas} + u_{\rm rad}$ is the sum of the gas, $u_{\rm gas}$, and radiation, $u_{\rm rad}$, internal energies.

3. Physical Setup

To study the effect of disk tearing in a highly warped accretion disk we evolve our model in two stages. In both stages we assume a rapidly spinning BH of mass $M_{\rm BH} = 10\,M_\odot$ and dimensionless spin $a = 0.9375$. The initial radial (r) and vertical (z) density profile of the disk is $\rho(r, z) \propto r^{-1} \exp(-z^2/2h^2)$. The disk extends from an inner radius, $r_{\rm in} = 6\,r_g$, to the outer radius, $r_{\rm out} = 76\,r_g$ at a constant scale height of $h/r = 0.02$. The covariant magnetic vector potential is $A_\theta \propto (\rho - 0.0005) r^2$ and normalized to give an approximately uniform $\beta = p_b/p_{\rm tot} \sim 7$ in the initial conditions. Here p_b is the magnetic pressure and $p_{\rm tot}$ is the sum of the electron/ion pressures, $p_{e,i}$, and the radiation pressure, $p_{\rm rad}$. This rather low value of $\beta \sim 7$ was chosen such that the grid is able to resolve both the toroidal and poloidal MRI wavelengths for a physically meaningful runtime. Parameter exploration considering higher β values will become possible in the coming 5–10 yr after the advent of (post-)exascale GPU clusters. The whole setup is subsequently rotated by 65° with respect to the BH spin axis, which itself is aligned with the polar axis of the grid. The physical equivalence between tilting the disk (e.g., Liska et al. 2018; White et al. 2019) and tilting the BH (e.g., Fragile & Anninos 2005; Fragile et al. 2007) is demonstrated in the Appendix of Liska et al. (2018).

In the first stage (model T65), which is described in Liska et al. (2022b), we evolve the disk in ideal GRMHD for $\Delta t = 150{,}000\,r_g/c$ with a preset scale height of $h/r = 0.02$ set by a cooling function (Noble et al. 2009). The disk undergoes a large tearing event around $t \sim 45{,}000\,r_g/c$, which is analysed in Musoke et al. (2023). During this tearing event a sub-disk of size $\Delta r \sim 10$–$15\,r_g$ tears off and precesses for ~six periods between $t \sim 45{,}000\,r_g/c$ and $t \sim 80{,}000\,r_g/c$. While precessing, the inner disk exhibits a very prominent radial epicyclic oscillation at $\nu = 56$ Hz for a 10 solar mass BH. Another tearing event between $t \sim 120{,}000\,r_g/c$ and $t \sim 145{,}000\,r_g/c$ produces a similar oscillation albeit at a slightly higher frequency of $\nu = 69$ Hz. These frequencies are consistent with observed high-frequency QPOs (e.g., Ingram & Motta 2019).

In the second stage (model RADT65), which is the focus of this work, we restart this simulation in full radiative GRMHD at $t = 29{,}889\,r_g/c$ as described above. The resolution is downscaled by a factor of two to reduce the cost of the simulation and make it amenable to the pre-exascale GPU cluster OLCF Summit on which this simulation has been run. This is well before the occurrence of any large tearing event in stage 1. We assume thermodynamic equilibrium between the gas and radiation by setting $T_r = T_e = T_i$ in the initial conditions and run this model (RADT65) for $\Delta t \sim 14{,}000\,r_g/c$ until $t \sim 45{,}000\,r_g/c$. The density scaling is set such that the average accretion rate corresponds to approximately $\dot{M}/\dot{M}_{\rm Edd} \sim 0.35$ with $\dot{M}_{\rm Edd} = \frac{1}{\eta_{\rm NT}} L_{\rm Edd} \big/ c^2$ the Eddington accretion rate, $L_{\rm Edd} = \frac{4\pi G M_{\rm BH}}{c \kappa_{\rm es}}$ the Eddington luminosity, and $\eta_{\rm NT} = 0.179$ the Novikov & Thorne (1973) efficiency. According to Piran et al. (2015) this choice of parameters is roughly consistent with a thin disk solution (Sadowski 2011) of scale height of $h/r = 0.02$–0.06 between $r = r_{\rm isco}$ and $r = 100\,r_g$.

4. Results

4.1. Tearing Process

The disk in RADT65 undergoes a tearing event between $t = 31{,}000\,r_g/c$ and $t = 40{,}000\,r_g/c$, as visualized using a 3D density isocontour rendering at three different times in Figure 1. Figure 2 shows a spacetime diagram, in which we calculate the average density of the disk $\bar{\rho} = \frac{\int_0^{2\pi}\int_0^{\pi} \rho^2 \sqrt{-g}\, d\theta d\phi}{\int_0^{2\pi}\int_0^{\pi} \rho \sqrt{-g}\, d\theta d\phi}$ (Figure 2(a)), the warp amplitude, $\Psi = r\frac{\partial \vec{l}}{\partial r}$ with $\vec{l}$ being the angular momentum (Figure 2(b)), the average electron and ion temperatures, $T_{e,i} = \frac{\int_0^{2\pi}\int_0^{\pi} p_{e,i} \sqrt{-g}\, d\theta d\phi}{\int_0^{2\pi}\int_0^{\pi} \rho \sqrt{-g}\, d\theta d\phi}$ (Figures 2(c) and (d), respectively), and the tilt and precession angles, $T_{\rm disk}$ and $P_{\rm disk}$ (Figures 2(e) and (f), respectively, as calculated in Fragile & Anninos 2005).

During this tearing event the disk precesses for $\lesssim$two periods between $36{,}000 < t < 38{,}000\,r_g/c$ (Figure 2(e)) before it aligns with the spin axis of the BH (Figure 2(f)). Alignment happens through warp-driven dissipation of misaligned angular

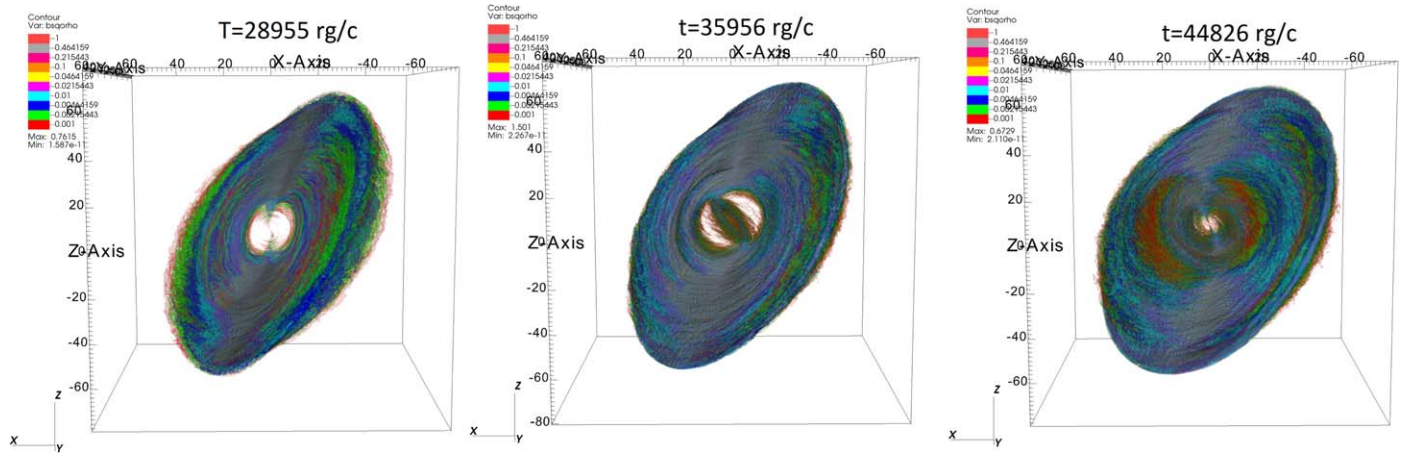

Figure 1. The first demonstration of disk tearing in a radiation-pressure-supported accretion disk, as seen through isocountour 3D renderings of the density at three different times. Left panel: the disk at $t = 28{,}955\ r_g/c$ forms a rigid body that is warped, but shows no differential precession. Middle panel: the disk tears off a precessing inner disk at $t = 31{,}000\ r_g$ that precesses for two periods between $t = 35{,}000\ r_g/c$ and $t = 37{,}000\ r_g/c$. While precessing, the inner disk aligns with the BH, shrinking in size until it fully disappears. Right pane: the disk forms a new tear at $r \sim 25\ r_g/c$ around $t \sim 45{,}000\ r_g/c$, and the tearing process repeats.

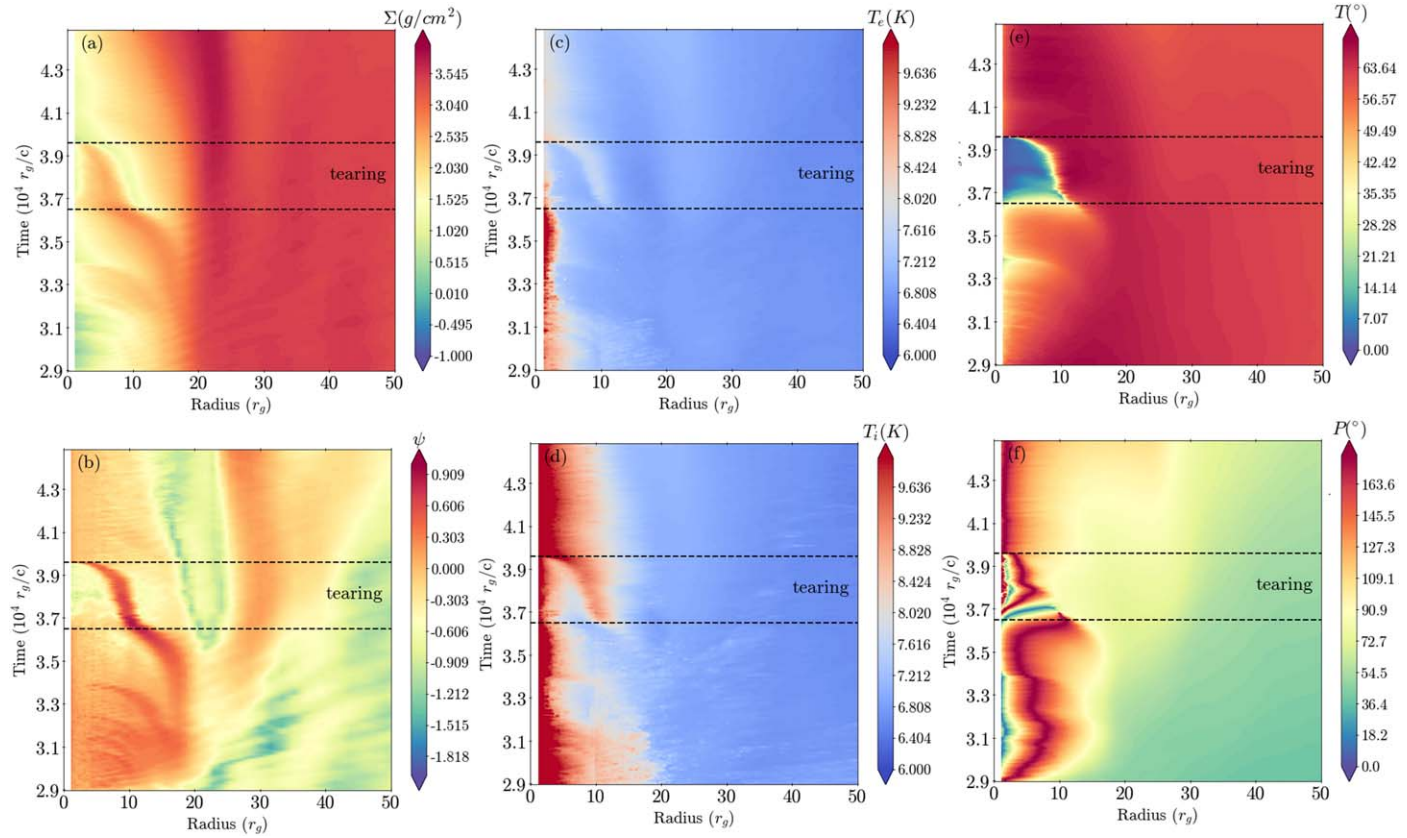

Figure 2. Panels (a) and (b): spacetime diagrams of the density, ρ, and warp amplitude, ψ. The warp amplitude peaks where the disk is about to tear or has already torn. Since dissipation is enhanced in warps, a maximum in the warp amplitude correspond to a minimum in the density. The main tearing event is denoted by black dotted lines. Panels (c) and (d): spacetime diagrams of the electron, T_e, and ion, T_i, temperatures. The ion and electron temperatures correlate with the warp amplitude and anticorrelate with the density. Close to the BH and in the tear the ions are significantly hotter than the electrons since Coulomb collisions are unable to equilibrate the ion and eletron temperatures. Panels (e) and (f): spacetime diagrams of the tilt, $\mathcal{T}$, and precession, $\mathcal{P}$, angle of the disk. Around $t \sim 36{,}500\ r_g/c$ a disk tears off and precesses for $\lesssim$two periods, during which it gradually aligns with the BH spin axis.

momentum on the accretion time of the inner disk, which differs from the Bardeen–Petterson alignment (Bardeen & Petterson 1975) mechanism that manifests itself on much shorter timescales during which the structure and density of the disk remains in a steady state (see the discussion in Liska et al. 2019b). In addition to this "main" tearing event there are indications, such as the formation of an inwards moving ring-like structure and an increase in the warp amplitude around $r \sim 30\ r_g$, that a much larger tearing event will occur after the end of this simulation. Due to the large

computational expense associated with extending the duration of RADT65, we leave the analysis of this (potentially) much longer tearing event to future work.

Whether a disk is able to tear depends on how the internal torques in the disk react to differential Lense–Thirring (LT) precession (e.g., Nixon & King 2012). The LT precession rate of a point particle around a rapidly spinning BH follows a steep radial dependence of $\nu_{\rm LT} \propto a/r^3$. However, an accretion disk will precess with a single frequency set by the integrated LT torque in the disk if the viscous torques are able to counteract the differential precession rate (e.g., Fragile & Anninos 2005; Fragile et al. 2007). Naively, one expects that the warp amplitude decreases monotonically with increasing distance from the BH. This is (roughly) the case in the inner and outer disk of RADT65 for $t \lesssim 32{,}000\, r_g/c$.

As Figures 2(a) and (b) show, the warp amplitude and surface density in RADT65 are anticorrelated for the entire runtime. At $r \lesssim 20\, r_g$ the warp amplitude is rather high and a cavity of low-density gas forms at both early and late times. In this cavity the plasma thermally decouples into hot electrons with $T_e \sim 10^8$–10^9 K and extremely hot ions with $T_i \sim 10^9$–10^{10} K. The strong anticorrelation between the warp amplitude and density suggests that accretion is driven by dissipation in warps (e.g., Papaloizou & Pringle 1983; Ogilvie 1999; Nelson & Papaloizou 2000). In a companion paper (Kaaz et al. 2022) we demonstrate that warp-driven dissipation is responsible for the bulk of the dissipation and that MRI-driven turbulence (e.g., Balbus & Hawley 1991, 1998) plays only a very subdominant role.

However, after $t \gtrsim 32{,}000\, r_g/c$ the warp amplitude is not a monotonically decreasing function of radius. Instead, the warp amplitude forms local minima and maxima, and concentric rings of higher density gas centered at the (local) minima of the warp amplitude form. It is known that when the warp amplitude exceeds a critical value, it can become unstable (Doğan et al. 2018; Doğan & Nixon 2020). When this happens, the viscous torques in the warp drop to zero and the disk tears. In RADT65 the tearing process starts at $r \sim 19\, r_g$ around $t \sim 33{,}000\, r_g/c$ and the disk fully detaches at $r \sim 10\, r_g$ around $t \sim 36{,}500\, r_g/c$. We see later that during this process warp-driven dissipation leads to a temporary burst in the BH accretion rate and luminosity around $t \sim 36{,}500\, r_g/c$ (Section 4.3). The disk even (briefly) enters the slim disk regime where $\dot{M} \sim \dot{M}_{\rm edd}$ and $L \sim 0.5\, L_{\rm edd}$, suggesting the luminosity is slightly suppressed due to photon trapping (e.g., Abramowicz et al. 1978).

As the gas from the inner disk falls onto the BH it transports angular momentum outwards. Angular momentum conservation dictates that the radius of the inner disk should increase. This process, called viscous spreading, affects all finite-size accretion disks that are not resupplied externally with gas (e.g., Liska et al. 2018; Porth et al. 2019). However, the inner disk in RADT65 does not spread viscously, but, in fact, decreases in size. This discrepancy could potentially be explained by cancellation of misaligned angular momentum (e.g., Nixon & King 2012; Hawley & Krolik 2018). Namely, when gas from the outer disk falls onto the inner disk the misaligned components of angular momentum cancel out leading to a net decrease in the inner disk radius. In addition, it is possible that the inner disk transfers some of its excess angular momentum to the outer disk. In a companion paper (Kaaz et al. 2022) we quantify the relative contributions of the angular momentum cancellation and outward angular momentum transport to the evolution of the tearing radius.

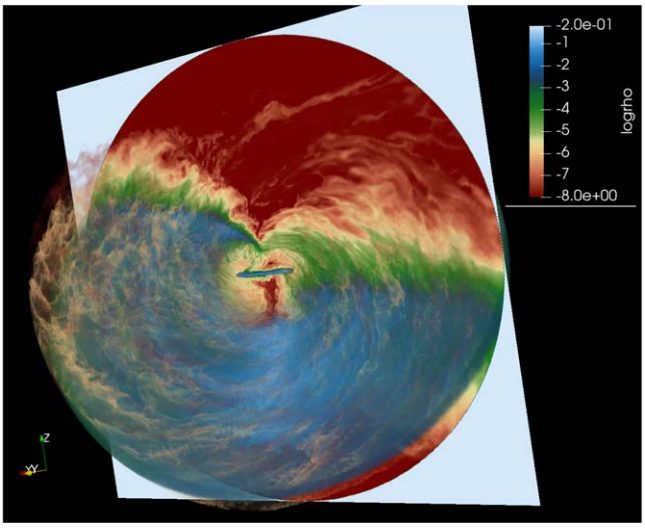

Figure 3. A volume rendering of the density during the main tearing event at $t = 37{,}026\, r_g/c$. The red plane cuts the disk at the $\phi = 0$ surface. Streamers from the outer disk (green) deposit low-angular-momentum gas onto the inner disk (blue). This causes the inner accretion disk to shrink in size (Kaaz et al. 2022).

4.2. Dissipation and Radiative Signatures

To understand better the structure of the disk during the tearing event at $t = 37{,}026\, r_g/c$ we show a volume rendering of the density in Figure 3 and a vertical projection of several quantities in Figure 4. In this projection the line of nodes, where the disk crosses the equatorial plane, is aligned with the horizontal x-axis. The projected quantities include the surface density $\Sigma = \int_0^\pi \rho \sqrt{g_{\theta\theta}}\, d\theta$ (panel (a)), the scattering optical depth $\tau_{\rm es} \sim 0.34\, \Sigma$ (panel (b)), electron and ion temperature $T_{e,i} = \frac{\int_0^\pi p_{e,i} \sqrt{g_{\theta\theta}}\, d\theta}{\Sigma}$ (panels (c) and (d), respectively), density scale height $\theta_d = \frac{\int_0^\pi \rho (\theta - \pi/2) \sqrt{g_{\theta\theta}}\, d\theta}{\Sigma}$ (panel (e)), effective bolometric luminosity $\lambda = \frac{\int_0^\pi R^r_t \sqrt{g_{\theta\theta}}\, 2\pi d\theta}{L_{\rm edd}}$ (panel (f)), gas entropy per unit mass $s_{\rm gas} = \frac{\int_0^\pi p_{e,i} / \rho^\gamma \rho u^t \sqrt{g_{\theta\theta}}\, d\theta}{\Sigma}$ (panel (g)), and radiation entropy per unit mass $s_{\rm rad} = \frac{\int_0^\pi E_{\rm rad}^{3/4} \sqrt{g_{\theta\theta}}\, d\theta}{\Sigma}$ (panel (h)). Integration is performed in a spherical coordinate system aligned with the local angular momentum vector of the disk. An animation of Figure 3 and panels (a), (c), and (f) of Figure 4 can be found on our YouTube channel (movie).

Interestingly, the electron and ion temperatures do not decline smoothly with distance from the BH (Figures 4(b) and (c), respectively) as predicted by idealized models of thin accretion disks Novikov & Thorne (1973). At a tearing radius of $10\, r_g$, where the warp amplitude reaches a maximum, the electron temperature reaches $T_e \gtrsim 10^8$ K and the plasma becomes optically thin. Here streamers of gas get thrown onto highly eccentric orbits and subsequently rain down on the inner disk (Figure 3). The rapid rise in temperature in the tear suggests that gas crossing the tear is subject to additional dissipation as it undergoes a rapid orbital plane change (see also Nixon & Salvesen 2013; Raj & Nixon 2021). If we assume the gas has a temperature of $T_i = 0$ K before crossing the tear at

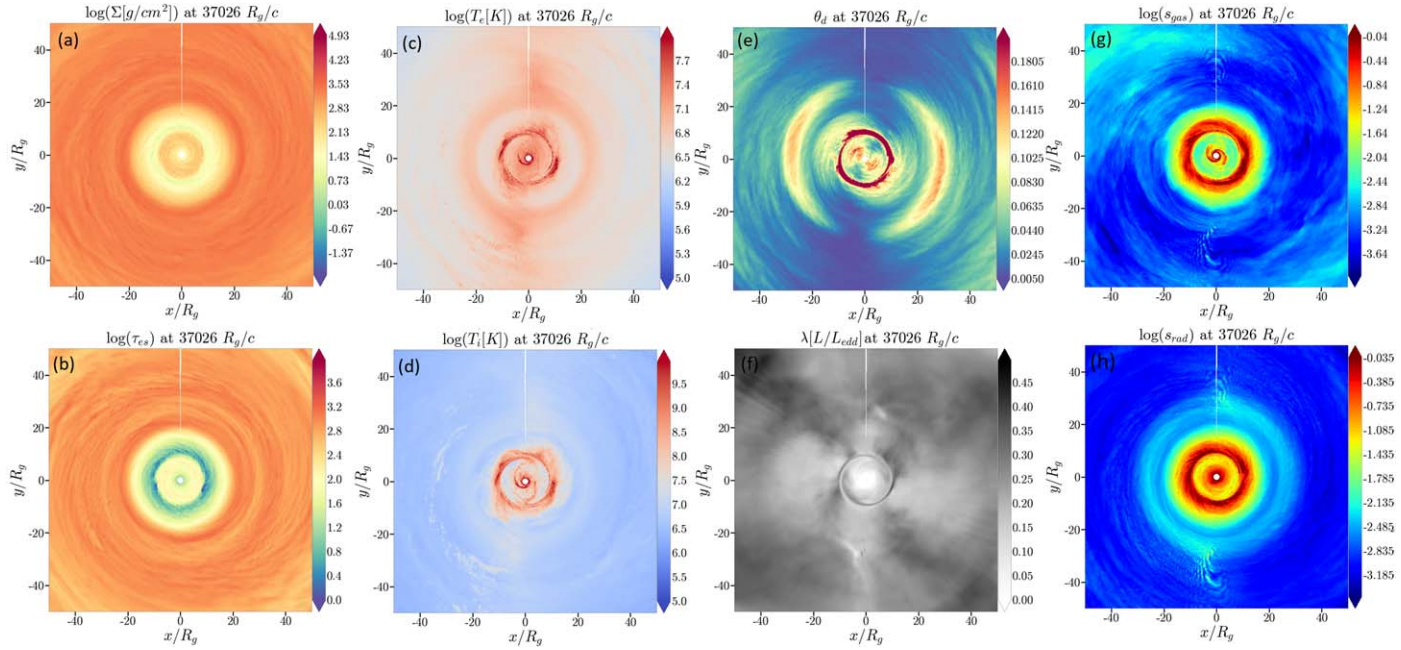

Figure 4. A top down view of the accretion disk during the main tearing event at $t = 37{,}026\ r_g/c$ corresponding to the volume rendering in Figure 3. Panel (a): the surface density, Σ, drops sharply in the tear due to additional dissipation as the gas undergoes a radical plane change. Panel (b): the vertically integrated scattering optical depth (τ_{es}) drops below unity in the tear suggesting optically thin emission. Panels (c) and (d): the electron, T_e, and ion, T_i, temperatures peak perpendicular to the line of nodes (due to a "nozzle" shock, see Section 4.2) and in the tear at $r \sim 10\ r_g$. Panel (e): the density scale height, θ_d, of the accretion disk oscillates azimuthally. It peaks along the x-axis and reaches a minimum along the y-axis. Panel (f) the bolometric luminosity, λ, forms a non-axisymmetric pattern ranging from $\lambda \sim 0.15\ L_{\rm Edd}$ to $\lambda \sim 0.5\ L_{\rm Edd}$. Panels (g) and (h): the gas entropy entropy, $s_{\rm gas}$, does not increase substantially when gas crosses the scale height compression along the vertical y-axis, but the radiation entropy, $s_{\rm rad}$, does. This suggests the shock heating is radiatively efficient.

$r \sim 7\ r_g$, and the gas dissipates $\epsilon = 10^{-2}$ of its orbital kinetic energy $U_{\rm kin} \approx \frac{1}{2r}$, we find that dissipation can easily heat the gas to $T_i \sim 10^{10}$K. In reality, ϵ can be much higher if radiative cooling is efficient.

The scale height of the disk exhibits a prominent $m = 2$ azimuthal oscillation (Figure 4(e)). This can also be observed in Figure 5 where we show a $\theta-\phi$ slice at $r = 25\ r_g$ of the density, electron temperature, and gas entropy. At the line of nodes the scale height reaches a maximum of $h/r \sim 0.1$, while perpendicular to the line of nodes the scale height drops to $h/r \sim 0.005$. Around this nozzle-like "compression," the gas reaches a temperature ranging from $T_e \sim 2 \times 10^7$ K at $r \sim 20\ r_g$ to $T_e \gtrsim 10^8$ K within $r \lesssim 5\ r_g$. At select times T_e can even reach $T_e \sim 10^9$ K closer to the BH (see this YouTube movie). The radial and azimuthal fluctuations in the temperature lead to a highly non-axisymmetric emission pattern (Figure 4(f)). At this specific snapshot ($t = 37{,}026\ r_g/c$) the effective bolometric luminosity varies azimuthally between $\lambda \sim 0.15\ L_{\rm edd}$ and $\lambda \sim 0.5\ L_{\rm edd}$ at $r = 200\ r_g$.

The specific gas entropy does not increase in the nozzle (Figure 4(g)), suggesting that the heating of gas in the nozzle is adiabatic. This might seem surprising since nozzles in tidal disruption events (TDEs) are typically associated with shock heating and steep gradients in the gas entropy (e.g., Rees 1988; Kochanek 1994; Andalman et al. 2022). However, if the radiative cooling timescale is very short, shocks do not automatically lead to an increase of the gas entropy. Instead, they will lead to an increase in the radiation entropy. This increase in radiation entropy is visible along the vertical y-axis in Figure 4(g). In a companion paper (Kaaz et al. 2022), we demonstrate that a shock forms in the nozzle that dissipates roughly ∼1.8% of the orbital energy each time the gas passes through it.

4.3. Outflows and Variability

To understand the variability associated with disk tearing and the energetics of the outflows we plot in Figure 6 the mass accretion rate (panel (a)), radiative emission rate (panel (b)), and (radiative) outflow efficiencies (panel (c)). The mass accretion rate measured at the event horizon ($\dot{M} = \int_0^{2\pi}\int_0^{\pi} \rho u^r \sqrt{-g}\, d\theta d\phi$, with g the metric determinant and u^μ the fluid 4-velocity) exhibits a factor ∼40 variation in time, ranging from $\dot{M} = 2 \times 10^{-2}\dot{M}_{\rm Edd}$ to $\dot{M} = \dot{M}_{\rm Edd}$ (defined in Section 3). However, the luminosity ($L = \int_0^{2\pi}\int_0^{\pi} R_t^r \sqrt{-g}\, d\theta d\phi$, with R_t^r the r–t component of the radiation stress energy tensor) only exhibits a factor ∼5 variation and peaks at $L \sim 0.5\ L_{\rm edd}$.

The outflow efficiencies with respect to the BH mass accretion rate are defined at the event horizon as $\eta_{\rm wind} = \frac{\dot{M} - \dot{E}}{|\dot{M}|_t}$, $\eta_{\rm rad} = \frac{L_{r=r_{200r_g}}}{|\dot{M}|_t}$, and $\eta_{\rm adv} = \frac{-L_{r=r_{\rm BH}}}{|\dot{M}|_t}$. Here $\dot{E} = \int_0^{\pi}\int_0^{2\pi} T_t^r \sqrt{-g}\, d\theta d\phi$ is the energy accretion rate with T_t^r the and $|\dot{M}|_t$ average of $\dot{M}$ over a time interval of $500\ r_g/c$. Unless stated otherwise, we measure $\dot{M}$ and $\dot{E}$ at the event horizon, and L at the event horizon for $\eta_{\rm adv}$ and at $r = 200\ r_g$ for $\eta_{\rm rad}$. As Figure 6(c) shows, when the accretion rate reaches the Eddington limit the advective efficiency, $\eta_{\rm adv}$, is of comparable magnitude to the radiative efficiency, $\eta_{\rm rad}$ (Figure 6(d)). This implies that a significant fraction of the emitted radiation will fall into the BH before it reaches the observer, suggesting the disk might have entered the slim disk regime at the peak of luminosity. Nevertheless, the time-averaged radiative efficiency reaches $|\eta_{\rm rad}| = 14.7\%$, which is only slightly below the canonical Novikov & Thorne (1973) efficiency of $\eta_{\rm NT} = 17.8\%$.

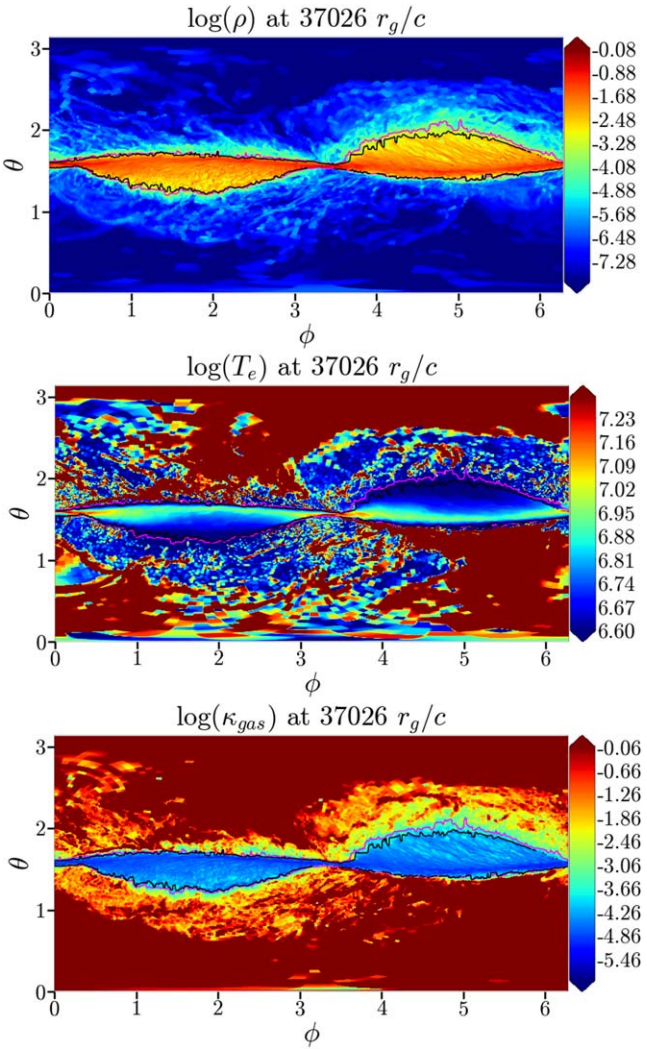

Figure 5. A $\theta-\phi$ slice through the disk at $r = 15\,r_g$ in tilted coordinates with the ascending node at $\phi = 1/2\pi$ and the descending node at $\phi = 3/2\pi$. The pink and black lines correspond to the $\tau_{es} = 1$ and $\tau_{bf} = 1$ surfaces, respectively. Upper panel: the gas density, ρ, peaks in the "nozzle", which is located perpendicular to the local line of nodes at $\phi = 0$ and $\phi = \pi$. Middle panel: the electron temperature, T_e, increases by a factor $\sim$5 in the nozzle, suggesting the radiative emission will be hardened. Lower panel: the gas entropy per unit mass, $\kappa_{\rm gas}$, does not increase in the nozzle, suggesting the rise in gas temperature is adiabatic (Section 4.2).

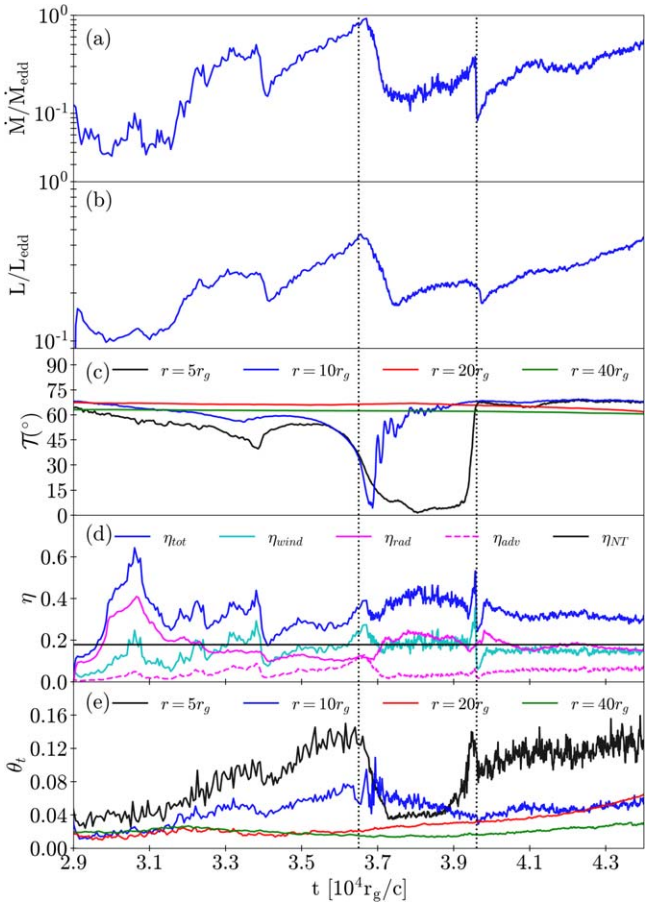

Figure 6. Time evolution of RADT65 with the main tearing event denoted by black dotted lines. Panel (a): the mass accretion rate increases from $\dot{M} \sim 10^{-2}\dot{M}_{\rm Edd}$ to $\dot{M} \sim 1\dot{M}_{\rm Edd}$. Panel b: the luminosity increases from $L \sim 0.1\,L_{\rm Edd}$ to $L \sim 0.5\,L_{\rm Edd}$. Panel (c): the tilt $\mathcal{T}$ of the accretion disk. The inner accretion disk ($r \lesssim 10\,r_g$) aligns with the BH just after the main tearing event while the outer accretion disk remains misaligned. Panel (d): the wind efficiency, $\eta_{\rm wind}$, radiative efficiency, $\eta_{\rm rad}$, advective radiative efficiency, $\eta_{\rm adv}$, Novikov & Thorne (1973) efficiency, $\eta_{\rm NT}$, and total efficiency, $\eta_{\rm tot}$, as defined in Section 4.3. When the accretion rate peaks, advection of radiation becomes important and suppresses the total luminosity of the system. Panel (e): the thermal scale height of the disk, θ_t, stays stable or increases throughout the disk, which suggests the disk is thermally stable (Section 4.5).

We do not observe any evidence for a radiation- or magnetic-pressure-driven wind. While the outflow efficiency measured at the event horizon exceeds $\eta_{\rm wind} \gtrsim 15\%$, this drops to $\eta_{\rm wind} \lesssim 0.1\%$ when measured at $r = 200\,r_g$, which demonstrates that both the magnetic pressure (e.g., Liska et al. 2019b) and radiation pressure (e.g., Kitaki et al. 2021) are insufficient to accelerate the wind to escape velocities. This suggests that poloidal magnetic fields are a key ingredient to accelerate subrelativistic outflows, even when the accretion rate approaches the Eddington limit.

4.4. Radial Structure

To understand the structure of the accretion disk better we show in Figure 7 time-averaged (between $t = [43{,}000, 44{,}000]\,r_g/c$) radial profiles of the density, $\bar{\rho}$ (panel (a)), luminosity, L (panel (b)), and radiation, ion, electron, and magnetic pressures, $p_{\rm rad}$, p_i, p_e, and p_b, respectively (panel (c)). During this time interval a new tear starts to form around $r \sim 30\,r_g$, which manifests itself as a drop in density and an increase in the radiative flux. While the magnetic and radiation pressures are in approximate equipartition within $r \lesssim 20\,r_g$, the accretion disk becomes fully radiation-pressure-dominated between $r = [20,\ 40]\,r_g$. The sum of the ion and electron pressure is a factor $\sim$10–100 lower than the radiation pressure, suggesting that gas pressure does not play a dynamically important role.

We have already mentioned in Section 4.1 that warp-driven dissipation plays an important role in RADT65. To illustrate how much warp-driven dissipation accelerates the inflow of gas in RADT65, we translate the radial infall speed of the gas into an effective viscosity, $\alpha_{\rm eff} = \frac{\langle v^r v^\phi \rangle_\rho}{\langle c_s^2 \rangle_\rho}$, with $v^r = u^r/u^t$ and $v^\phi = u^\phi/u^t$. Here, $\langle x \rangle_y = \frac{\int_0^{2\pi}\int_0^{\pi} xy\sqrt{-g}\,d\theta d\phi d\phi}{\int_0^{2\pi}\int_0^{\pi} y\sqrt{-g}\,d\theta d\phi}$ gives the y-weighted average of quantity x. In Figure 7(c), we find $\alpha_{\rm eff} \sim 1$–5×10^{1} throughout the disk. The Maxwell stresses $\alpha_{\rm m} = \frac{\langle b^r b^\phi \rangle_\rho}{\langle p_{\rm tot} \rangle_\rho} \sim 10^{-2}$–$10^{-1}$ induced by magnetized turbulence

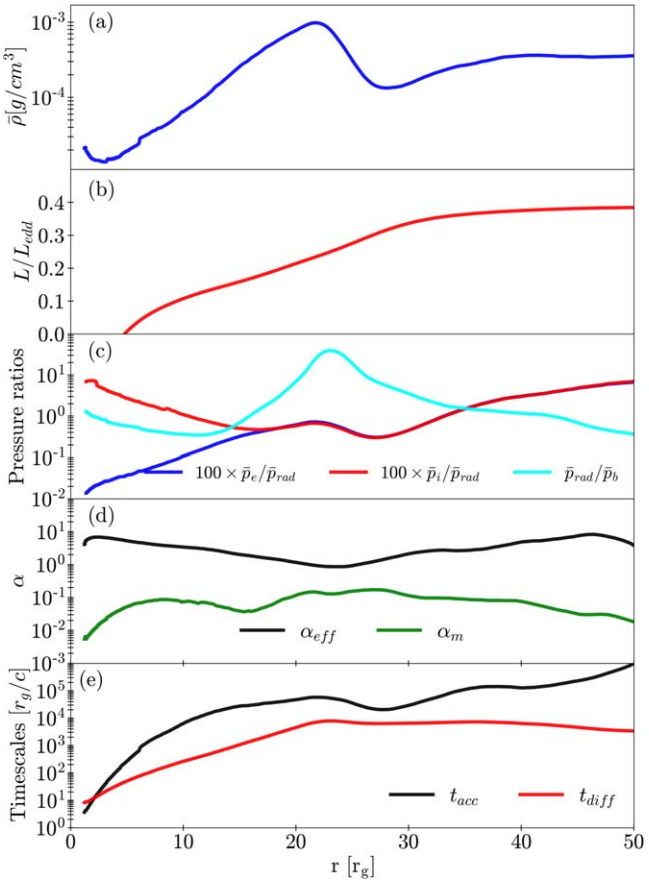

Figure 7. Radial structure of the disk time-averaged between $t = [43{,}000; 44{,}000]\, r_g/c$. This is the end state of our simulation at which point a new tear starts to form. Panel (a): the gas density, $\bar{\rho}$, peaks around $r \sim 25\, r_g$. We expect the new tear to form just behind the peak in density. Panel (b): the cumulative luminosity of the disk increases until $35\, r_g$, partially driven by enhanced dissipation in the forming tear between $r = 20\, r_g$ and $r = 30\, r_g$. Panel (c): the disk is radiation-pressure-dominated, $p_{\rm rad}$, between $r = [15, 40]\, r_g$ and magnetic-pressure-dominated, p_b, everywhere else. The ion, p_i, and electron, p_e, pressures are very weak compared to either the radiation or magnetic pressure and thus do not play an dynamically important role. Panel (d): the effective viscosity, $\alpha_{\rm eff}$, is much larger than the Maxwell, $\alpha_{\rm m}$, stress. This suggests that dissipation is not driven by magnetized turbulence induced by magnetic stresses. Instead, we demonstrate in a companion paper that shocks are driving accretion (Kaaz et al. 2022). Panel (e): the photon diffusion timescale, $t_{\rm diff}$, is shorter than the accretion timescale, $t_{\rm acc}$, except very close to the BH. This suggest that advection of radiation internal energy is only dynamically important very close to the BH.

cannot account for this effective viscosity, which suggests that other physical processes such as shocks (e.g., Fragile & Blaes 2008) drive accretion in warped accretion disks.

4.5. Thermal Stability

Interestingly, Liska et al. (2022a) found that an aligned version of the accretion disk in RADT65 collapsed within $t \lesssim 5000\, r_g/c$ to an exceedingly thin slab that could not be resolved numerically. This runaway cooling (see also Sądowski 2016; Fragile et al. 2018; Jiang et al. 2019; Mishra et al. 2022) is a manifestation of thermal instability (Shakura & Sunyaev 1976). However, we do not observe any evidence for thermal instability in RADT65. In fact, as Figure 6(e) demonstrates, the thermal scale height, $\theta_t = \frac{\langle c_s \rangle_\rho}{\langle v^\phi \rangle_\rho}$, remains stable or even increases depending on the radius.

This unexpected result could potentially be explained within $r \lesssim 20\, r_g$ by magnetic fields, which can stabilize a thermally unstable accretion disk if they reach equipartition with $p_b \sim p_{\rm rad}$ (e.g., Begelman & Pringle 2007; Sądowski 2016; Jiang et al. 2019; Liska et al. 2022a; Mishra et al. 2022). However, magnetic fields will not be able to stabilize the disk between $r = [20, 40]\, r_g$ where the disk is strongly radiation-pressure-dominated with $p_{\rm rad}/p_b \sim 10^1$–$10^2$.

We found in Section 4.3 that advection of radiation becomes significant at the event horizon. If the radiation diffusion timescale becomes longer than the accretion timescale, photon trapping might stabilize the disk against runaway cooling (e.g., Abramowicz et al. 1978). To test if photon trapping can explain the apparent thermal stability of the disk we plot the radiation diffusion time, $t_{\rm diff} \sim \frac{h}{v_{\rm rad}} \sim 3h\tau_{\rm es}$ and the accretion time, $t_{\rm acc} = \frac{r}{\langle v_r \rangle_\rho}$, in Figure 7(e). Here we use for $v_{\rm rad}$ the optically thick radiation diffusion speed $v_{\rm rad} \sim \frac{1}{3\tau_{\rm es}} c$ (e.g., McKinney et al. 2013). As is evident from Figure 7(e), while the radiation diffusion and accretion timescales are comparable in the inner disk, the radiation diffusion timescale becomes much shorter than the accretion timescale in the outer disk. This suggests that photon trapping will not be able to stabilize the outer disk against runaway cooling or heating.

Instead, we propose in Section 5 that nozzle-shock-driven accretion disks are inherently thermally stable.

5. Discussion

5.1. Applicability to Spectral States

The accretion disk in RADT65 does not launch any relativistic jet. This suggests RADT65 is applicable to the high-soft and potentially soft-intermediate spectral states. In these spectral states the spectrum is dominated by thermal blackbody radiation and no radio jets are detected (though see Russell et al. 2020 for the detection of compact jets in the infrared).

Nevertheless, the emission profile of RADT65 presents a radical departure from the Novikov & Thorne (1973) model of a thin accretion disk. Instead of an axisymmetric power-law emission profile, emission in warped accretion disks can become hardened around the nozzle shock or at the tearing radius (see also Nixon & Salvesen 2013; Raj & Nixon 2021). Here the temperature of plasma can reach $T_e \sim 10^8$–10^9 K, which might lead to the Comptonization of cold accretion disk photons. This could potentially contribute to the high-energy power-law emission tail observed in the spectra of soft state BHXRBs (e.g., Remillard & McClintock 2006) in addition to the soft X-Ray excess in the spectra of high-luminosity AGNs (e.g., Gierlinski & Done 2004, 2006). Note that part of this high-energy emission can come from within the innermost stable circular orbit (ISCO) as suggested by recent GRMHD simulations (Zhu et al. 2012) and semi-analytical models (Hankla et al. 2022). Future general relativistic ray-tracing (GRRT) calculations will need to quantify how much the spectrum deviates from a blackbody spectrum and in which wavelength bands this optically thin shock-heated gas can be detected. The energy spectrum of the accelerated electrons will depend on the microphysics of the shocks, which will need to be addressed by particle-in-cell simulations.

In the hard-intermediate state (HIMS) jetted ejections imply that the accretion disks might be saturated by vertical magnetic

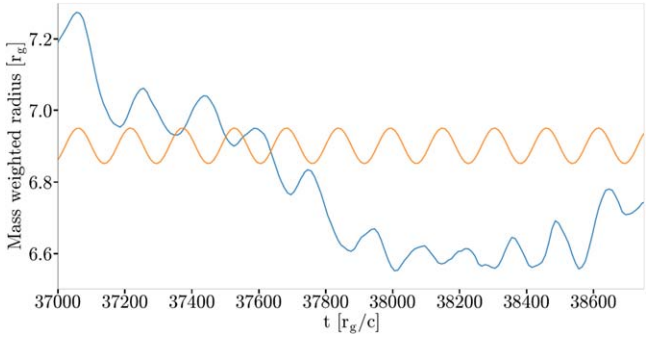

Figure 8. The mass-weighted radius, $r_M = \frac{\int_0^{2\pi}\int_0^{\pi}\Sigma r^3\sqrt{-g}\,d\theta d\phi}{\int_0^{2\pi}\int_0^{\pi}\Sigma r^2\sqrt{-g}\,d\theta d\phi}$, of the inner disk (after tearing) in RADT65 (blue) features a radial epicyclic oscillation consistent with the radial epicyclic frequency of an oscillating ring of gas at $r = 6.9\,r_g$ (orange). Such oscillations may be associated with high-frequency QPOs detected in BHXRB light curves.

flux (e.g., Tchekhovskoy et al. 2011; McKinney et al. 2012; Chatterjee et al. 2020). When an accretion disk is saturated by magnetic flux it enters the magnetically arrested disk (MAD) regime (Narayan et al. 2003) in which magnetic pressure overcomes gravity and accretion proceeds through non-axisymmetric instabilities. Recent two-temperature radiative GRMHD simulations (Liska et al. 2022a) have demonstrated that magnetic flux saturation can lead to "magnetic" truncation during which the inner disk decouples into a magnetic-pressure-supported "corona" of hot electrons ($T_e \gtrsim 5\times10^8$ K) and extremely hot ions ($T_i \gtrsim 10^{10}$ K). This happens within the magnetic truncation radius, which is determined by the amount and location of the excess poloidal magnetic flux in the system. It is conceivable that the combined effects of magnetic reconnection in current sheets and shocks in warps can heat the plasma to temperatures far above what was observed in this work or in Liska et al. (2022a). Future work will need to address if, where, and how such misaligned truncated disks tear, and if their spectral and timing signatures are consistent with sources in the HIMS.

5.2. Quasi-periodic Variability

This work and Musoke et al. (2023) have demonstrated that disk tearing can lead to short luminosity outbursts of length $\Delta t \sim 1000$–$3000\,r_g/c$ every $\Delta t_{\rm tear} \sim 10{,}000$–$50{,}000\,r_g/c$. Coincident with a tearing event the disk precesses on a timescale of $\Delta t_{\rm prec} \sim 1000$–$6000\,r_g/c$ suggesting tearing events might be accompanied by a sinusoidal modulation of the light curve. In parallel, the mass-weighted radius of the precessing inner disk oscillates on a timescale of $\Delta t_{\rm osc} \sim 150$–$400\,r_g/c$ suggesting another sinusoidal modulation of the light curve albeit at a higher frequency (Figure 8 and Musoke et al. 2023). We summarize the timescales of these variability phenomena in Table 1 for a BHXRB ($M_{\rm BH} = 10\,M_\odot$), a low-mass AGN ($M_{\rm BH} = 10^6\,M_\odot$), and a high-mass AGN ($M_{\rm BH} = 10^9\,M_\odot$). Please note that these timescales might vary by at least an order of magnitude depending the location of the tearing radius, which we expect will depend on, e.g., the accretion rate, BH spin, misalignment angle, and amount of large-scale magnetic flux.

Table 1 suggests that the timescales associated with disk tearing are consistent with a variety of astrophysical phenomena (see also Nixon & Salvesen 2013; Raj & Nixon 2021). The tearing events themselves might be associated with the heartbeat modes (on 1–100 s timescales) detected in the

Table 1
Time Period between Large Tearing Events, $\Delta t_{\rm tear}$, Disk Precession Period, $\Delta t_{\rm prec}$, and Period of Radial Epicyclic Oscillations, $\Delta t_{\rm osc}$, for Various BH Masses

$M_{\rm BH}$	$\Delta t_{\rm tear}$	$\Delta t_{\rm prec}$	$\Delta t_{\rm osc}$
N/A	50,000 r_g/c	6000 r_g/c	400 r_g/c
$10M_\odot$	2.5 s	0.3 s	20 ms
$10^6M_\odot$	70 hr	9 hr	0.5 hr
$10^9M_\odot$	8 yr	1 yr	20 days

Note. These timescales can be associated with variousvariability phenomena in BHXRBs and AGN such as QPEs, QPOs, and heartbeat oscillations (Section 5).

BHXRBs GRS 1915+105 and IGR J170913624 (e.g., Belloni et al. 2000; Altamirano et al. 2011; Neilsen et al. 2011; Weng et al. 2018) in addition to QPEs detected in various AGNs (e.g., Miniutti et al. 2019; Giustini et al. 2020; Arcodia et al. 2021; Miniutti et al. 2022). If the tearing events in some spectral states are spaced further apart, they could potentially also explain some changing-look phenomena observed in AGN with masses of 10^7–$10^9\,M_\odot$ that occur on timescales of years to decades (e.g., Sniegowska et al. 2020). In all of these cases the luminosity fluctuates by a factor 10^0–10^2, suggesting some significant flaring event in the accretion disk reminiscent of a tearing event. The precession of the disk that follows each tearing event can potentially explain low-frequency QPOs detected in numerous BHXRB with $\nu \sim 10^{-1}$–10^1 Hz (e.g., Ingram & Motta 2019). Precession is also consistent with the 44 day low-frequency QPO detected in the $2\times10^8\,M_\odot$ AGN KIC 9650712 (Smith et al. 2018) and the 3.8 hour low-frequency QPO detected in the 10^5–$10^6\,M_\odot$ AGN GJ1231+1106 (Lin et al. 2014). In addition, the oscillation of the mass-weighted radius might be associated with high-frequency QPOs of $\nu \sim 10^1 - 10^2$ Hz in BHXRBs and some of the short-duration QPOs detected in various AGNs. These include the $\sim$1 hour QPO in the light curve of the 10^6–$10^7\,M_\odot$ AGN RE J1034+396 (Gierlinski et al. 2008; Czerny et al. 2016), the 1.8 hour QPO in the $5\times10^6\,M_\odot$ MRK 766 (Zhang et al. 2017), and the 2 hour QPO in the $4\times10^6\,M_\odot$ AGN MS 2254.9–3712 (Alston et al. 2015).

The heated gas at the tearing radius suggests that QPO emission will be substantially hardened through Comptonization. This is consistent with frequency-resolved spectroscopy of BHXRBs, which has demonstrated that the Type-C QPO waveform is dominated by hardened emission (Sobolewska & Życki 2006) and recent observations of AGNs that suggest an increase in the soft X-ray excess during QPEs (Giustini et al. 2020). Interestingly, our simulations suggest that tearing events are accompanied by a low-frequency sinusoidal signal caused by precession of the inner disk and a high-frequency sinusoidal signal caused by a radial epicyclic oscillation at the tearing radius. This can potentially be tested using observational data for both BHXRBs and AGNs.

5.3. Comparison to Semi-analytical Models

Semi-analytical models typically divide warped accretion disks into two categories (e.g., Papaloizou & Pringle 1983) depending on the scale height of the disk relative to the α-viscosity parameter. In the first category bending waves excited

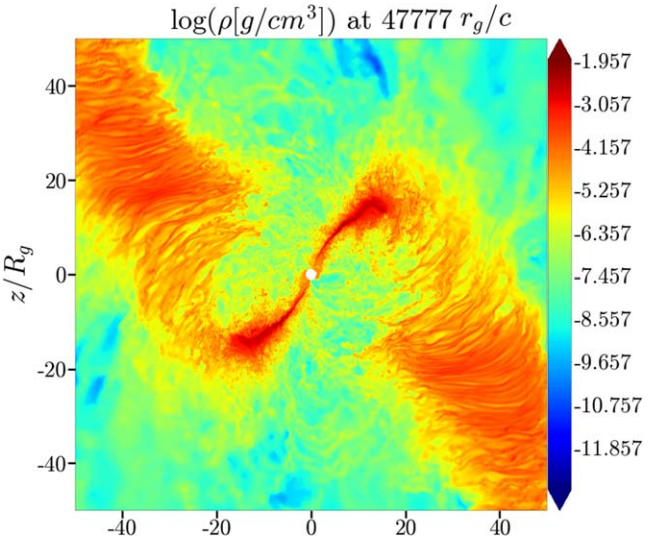

Figure 9. A transverse slice through the density along the line of nodes at 50 r_g. This snapshot is taken beyond the "official" duration of our simulation (Section 3), just after the onset of the next tearing event. Outwards propagating wave-like structures (visible as vertical "stripes") form in the outer disk suggesting that wave-like angular momentum transport might be present. The vertical extent of the outer disk is artificially inflated because the frame is sliced at an angle with respect to the disk.

by oscillating radial and vertical pressure gradients in the warp are damped and the warp is propagated through viscous diffusion only. This happens when the scale height is smaller than the viscosity parameter, e.g., $h/r < \alpha$. In this regime instability criteria were derived that predict the tearing of accretion disks (e.g., Ogilvie & Dubus 2001; Doğan et al. 2018; Doğan & Nixon 2020). In the second category the warp is propagated through bending waves that travel at a fraction of the sound speed (Papaloizou & Lin 1995). These bending waves are excited by pressure gradients in a warp. Past work has made substantial progress in describing warp propagation in the bending-wave regime (e.g., Ogilvie & Latter 2013; Paardekooper & Ogilvie 2018; Deng et al. 2020; Ogilvie 2022), and recently also addressed disk tearing in the bending-wave regime using SPH simulations and linearized fluid equations (Drewes & Nixon 2021).

Interestingly, Deng & Ogilvie (2022) predicted using the affine model of Ogilvie (2018) that oscillations in the vertical pressure gradient lead to an azimuthal $m = 2$ oscillation in the scale height of the disk similar to what is observed in our work. These authors also demonstrated that a parametric instability can induce turbulence and create ring-like structures in warped accretion disks. Since $h/r \sim \alpha_m$ (Figure 7(d)) and the warp is highly nonlinear it is unclear in which regime of warp propagation our disk falls (see also Sorathia et al. 2013; Hawley & Krolik 2018). We do note though that there is some evidence for wave-like structures in the disk (Figure 9), which suggests the disk might be in the bending-wave regime of warp propagation. Nevertheless, future work will need to isolate wave-like from diffusive (misaligned) angular momentum transport to make more direct comparison to semi-analytical models possible.

5.4. Thermal and Viscous Stability of Warped Disks

In Section 4.5 we demonstrated that warped, radiation-pressure-supported accretion disks remain thermally stable for much longer than similar non-warped, radiation-pressure-supported accretion disks considered in previous work (Liska et al. 2022a). We concluded that neither magnetic pressure nor advection of radiation internal energy can explain this thermal stability. Here we propose an alternative explanation.

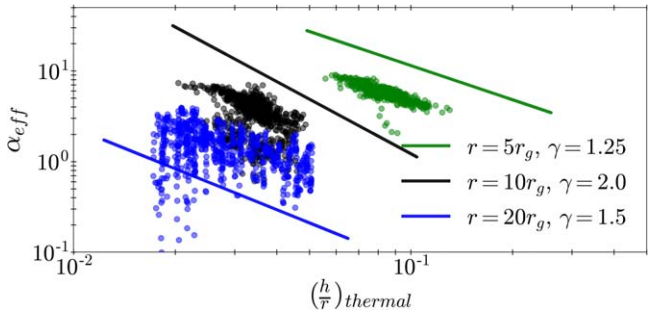

Figure 10. A scatterplot of the effective viscosity, $\alpha_{\rm eff}$, with respect to the thermal scale height, θ_t at $r = 5\ r_g$ in green, $r = 10\ r_g$ in black, and $r = 20\ r_g$ in blue. We show power-law fits to the data as solid lines with fitting function $\alpha_{\rm eff} \propto (h/r)^{-\gamma}$. The effective viscosity increases as the disk becomes thinner, which suggests warp-driven dissipation becomes more important for thinner disks. We argue in Section 5.4 that warp-driven dissipation can stabilize the disk against runaway thermal collapse (e.g., Shakura & Sunyaev 1976).

For a disk to remain thermally stable the derivative of the dissipation rate, $Q_{\rm vis}$, with respect to the temperature needs to be smaller than the derivative of the cooling rate, $Q_{\rm rad}$, with respect to the temperature such that $\frac{Q_{\rm vis}}{dT} < \frac{Q_{\rm rad}}{dT}$. For an α-viscosity radiation-pressure-supported disk, $Q_{\rm vis} \propto T^r_\phi H \propto \alpha p_{\rm tot} H \propto \alpha p^2_{\rm tot} \propto \alpha T^8$ and $Q_{\rm rad} \propto T^4$ (Shakura & Sunyaev 1973; Meier 2012). This suggests that with a constant α-viscosity, radiation-pressure-supported accretion disks are thermally unstable. However, if the dissipation rate follows $Q_{\rm vis} \propto T^\zeta$ with $\zeta \lesssim 4$ due to warping, the disk will remain thermally stable.

To determine ζ in our simulation we present in Figure 10 a scatterplot of the effective viscosity, $\alpha_{\rm eff}$, with respect to the thermal scale height, θ_t. We only use data after 32,000 r_g/c to allow the disk to adjust after seeding it with radiation and exclude data where the tilt angle is smaller than $\mathcal{T} < 60°$. We visually fit the data to find that $\alpha_{\rm eff} \propto H^{-\gamma}$ with $\gamma \sim 1.25$–1.75. From the relation $H \propto p_{\rm tot} \propto T^4$ we find that $\zeta = 8 - 4\gamma \sim 1$–$3$. This suggests that even though our accretion disk is radiation pressure dominated at $r = 20\ r_g$, warp-driven dissipation can potentially prevent the disk from becoming thermally unstable.

Following a similar argument, one can show that the warp-driven dissipation also avoids the viscous Lightman & Eardley (1974) instability of radiation-pressure-dominated disks. If the disk is subject to a viscous instability, it will disintegrate into rings of high-density gas (e.g., Mishra et al. 2016). Even though high-density rings do form in our simulation (Figures 2 and 4), we conclude that this cannot be a manifestation of viscous instability since similar rings form in the non-radiative analog to RADT65 presented by Musoke et al. (2023). This suggests that the ring formation in RADT65 is warp-induced.

5.5. Radiation Warping

When the inner disk precesses it will periodically beam radiation toward the outer disk. This can potentially warp the outer disk and induce additional dissipation (similar to Pringle 1997; Wijers & Pringle 1999). In a similar context Liska et al. (2021) has demonstrated that when a precessing jet collides with the outer accretion disk it can inject energy and angular momentum into the disk, leading to an increase of

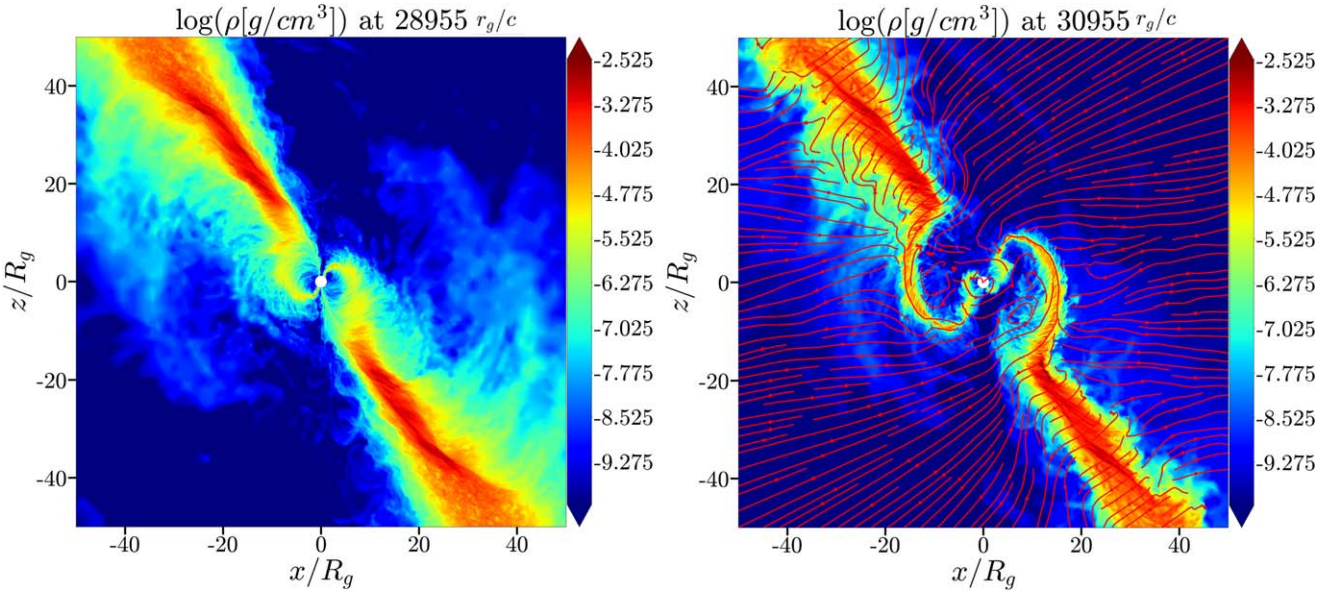

Figure 11. The radiation field warps the inner disk, as seen in a transverse slice of density through the $x-z$ plane of our initial conditions (left) and after $\Delta t = 2000\ r_g/c$ (right) with radiation streamlines shown in red. Even though our M1 radiation scheme is unable to model multi-beam radiation properly (Section 5.5), these results suggest that radiation warping might be an important effect.

particle orbits in the outer disk. Since the energy efficiency of the radiative outflows in RADT65 is non-negligible ($|\eta_{\rm rad}| \sim 14.7\%$) we expect that radiation feedback can have a profound effect on the structure and dynamics of an accretion disk.

Radiative feedback is an interesting avenue of future research that is hard to address in this article due to the limitations of our M1 radiation closure (Levermore 1984). M1 works well in modeling radiative cooling and energy transport in optically thick regions, and in optically thin regions for a single radiation bundle. However, M1 is unable to model crossing radiation bundles properly. The reason for this is that M1 treats radiation as a highly collisional fluid and is thus unable to model crossing radiation bundles in optically thin media. Instead the energy and momentum of the two radiation bundles will be summed together. While the M1 closure conserves the total amount of energy and momentum in the photon-fluid, it can lead to a nonphysical redistribution of energy and angular momentum.

Despite these limitations we demonstrate in Figure 11 that the structure of the inner accretion disk in RADT65 differs significantly after seeding it with radiation. In Figure 11 the radiation streamlines get deflected by the inner disk, presumably leading to an increase in the warp amplitude compared to the start of the simulation. In this snapshot the tearing process has not started yet, which suggests that radiation warping can be important even in the absence of disk tearing. While these preliminary results are encouraging, more advanced numerical simulations will be necessary to address radiation warping reliably.

5.6. Role of Magnetic Fields

In this work we have seeded the accretion disk with a relatively strong toroidal magnetic field of $\beta = \frac{p_{\rm gas}+p_{\rm rad}}{p_b} \sim 7$ (Section 3) in order to be able to resolve the poloidal MRI components and reach numerical convergence. Alternatively, we could have threaded the accretion disk with poloidal magnetic flux loops and chosen a higher plasma-β in the initial conditions as we have done in the past (e.g., Liska et al. 2021). However, this leads to the formation of powerful jets and would make these simulations more applicable to the hard-intermediate spectral state (e.g., Liska et al. 2022a).

In an accompanying paper (Kaaz et al. 2022) we demonstrate that the turbulent Maxwell stresses seeded by MRI turbulence fall short by 1–3 orders of magnitude in explaining the measured accretion rate. Instead, we demonstrate that accretion is driven by shock dissipation in the nozzle. This naively suggests that magnetic fields do not play an important role in the disk dynamics and thus that the presented results would be insensitive to the chosen plasma-β.

However, magnetic fields might still play an important role in communicating the differential LT torque throughout the accretion disk. This can have important consequences for the tearing process and the formation of the nozzle shock. In fact, SPH models (e.g., Nixon et al. 2012a, 2012b; Nealon et al. 2015; Raj et al. 2021), which do not include magnetic fields, find that a thin accretion disk tears apart into multiple deferentially precessing rings instead of a radially extended sub-disk observed in our GRMHD simulations. In addition, SPH models do not find a nozzle shock. These arguments suggest that magnetic fields might play an important, though indirect role, in both the tearing process and the formation of the nozzle shock, which needs to be addressed in future work.

5.7. Numerical Convergence

RADT65 is the largest radiative 2T GRMHD simulation to date, featuring on average over 3×10^9 cells, and requiring over 6000 V100 GPUs on OLCF Summit. Nevertheless, to reduce the numerical cost of this work and bring it within the realm of possibilities, we needed to downscale the resolution by a factor of two compared to similar work presented in Liska et al. (2022b) and Musoke et al. (2023), which did not take radiation into account. Despite this downscaling, the number of cells per MRI-wavelength, $Q^i = \lambda^i_{\rm MRI}/N^i$, still exceeds ($Q^\theta$,

$Q^{\phi}) \gtrsim (20, 125)$ and the number of cells per disk scale height, Z, exceeds $Z \gtrsim 14$.

This suggests, based on more controlled convergence studies (e.g., Shiokawa et al. 2012; Porth et al. 2019), that both the disk and the MRI turbulence are reasonably well resolved and close to achieving convergence. In fact, the vast majority of GRMHD simulations performed to date (e.g., Porth et al. 2019) have similar or even slightly inferior Q and Z parameters. In addition, physical quantities like the inflow speed of the gas and the evolution of the tearing radius, are very similar to the non-radiative GRMHD models in Liska et al. (2022b) and Musoke et al. (2023), suggesting the results presented in this article are robust and no significant qualitative changes are expected at higher resolutions.

Despite these arguments a full convergence study will be an interesting use case for future generations of GPU clusters. Namely, doubling the resolution is currently computationally infeasible. Doing so, would increase the cost of the presented simulations 16-fold to over 4 million node hours on OLCF Summit. This would exceed the size of our entire INCITE allocation by more than an order of magnitude. On the other hand, we already know based on previous convergence studies (e.g., Shiokawa et al. 2012; Porth et al. 2019) that reducing the resolution by a factor of two would under-resolve both the poloidal MRI components and the scale height of the disk, and thus fail to reach convergence.

6. Conclusion

In this article we have presented the first radiative two-temperature GRMHD simulation of an 65° misaligned disk accreting at $\dot{M} \sim 0.35\dot{M}_{\rm edd}$. Similar to the idealized GRMHD models presented in Liska et al. (2021, 2022b) and Musoke et al. (2023), the radiation-pressure-supported accretion disk tears apart and forms a precessing disk. During the tearing process the mass accretion rate increases by a factor ∼10–40 and the luminosity increases by a factor ∼5, almost exceeding the Eddington limit at the peak of the outburst. As proposed in Raj & Nixon (2021), the timescales and amplitudes of these luminosity swings are roughly consistent with the QPEs in AGN (e.g., Miniutti et al. 2019, 2022; Giustini et al. 2020; Arcodia et al. 2021) and several heartbeat modes in BHXRBs (e.g., Belloni et al. 2000; Altamirano et al. 2011; Neilsen et al. 2011; Weng et al. 2018). Following a tearing event, the inner disk precesses for several periods with a frequency that is consistent with low-frequency QPOs (e.g., Ingram & Motta 2019). While precessing, the inner disk also exhibits a radial epicyclic oscillation of its center of mass whose frequency is consistent with high-frequency QPOs (e.g., Ingram & Motta 2019). Future long-duration GRMHD simulations combined with radiative transfer calculations will need to test if disk tearing indeed produces QPO-like variability. This will require the tearing radius to remain stable over many cycles of tearing.

Warping of the disk forms two nozzle shocks directed perpendicular to the line of nodes. At the nozzle shock, the scale height of the disk decreases by a factor of ∼5 and the temperature increases up to $T_e \sim 10^8$–10^9 K and $T_i \sim 10^9$–10^{10} K. In a companion paper (Kaaz et al. 2022), we demonstrate that dissipation in the nozzle shock leads to a much shorter accretion timescale than predicted by α-viscosity-based models (e.g., Shakura & Sunyaev 1973) seeded by magnetized turbulence (e.g., Balbus & Hawley 1991). This can potentially explain the timescales associated with some changing-look phenomena in AGN including QPEs. In addition, we find during tearing events that gas crossing the tear heats up to $T_e \sim 10^8$ K and $T_i \sim 10^{10}$ K. This is caused by an increase in the dissipation rate as the gas undergoes a rapid orbital plane change (see also Nixon & Salvesen 2013; Raj & Nixon 2021). These results imply that the emission profile from warped accretion disks will deviate substantially from the Novikov & Thorne (1973) model of a geometrically thin accretion disk. This can, pending future radiative transfer calculations, have far-reaching consequences for spectral fitting and BH spin measurements (e.g., Zhang et al. 1997; Kulkarni et al. 2011).

While radiation-pressure-supported accretion disks in GRMHD simulations typically collapse (e.g., Sądowski 2016; Fragile et al. 2018; Jiang et al. 2019; Mishra et al. 2020; Liska et al. 2022a) into an infinitely thin slab due to thermal instability (Shakura & Sunyaev 1976), this did not happen in our simulation. Here we argue that the warp and associated nozzle shock stabilize the disk against thermal collapse (Section 5). These shocks differ from spiral density-wave-induced shocks (e.g., Arzamasskiy & Rafikov 2018). In a companion paper (Kaaz et al. 2022), we demonstrate that nozzle shock dissipation drives accretion in geometrically thin warped accretion disks within at least $r \lesssim 50\, r_g$. This upends the standard paradigm that invokes MRI-induced turbulence for the dissipation of orbital kinetic energy (e.g., Balbus & Hawley 1991, 1998). Future work will need to address the range of spectral states, accretion rates, and misalignment angles where nozzle shock dissipation becomes important.

Past work almost exclusively invoked magnetic reconnection in coronae to explain high-energy (non-)thermal emission from accretion disks (e.g., Sironi & Spitkovsky 2014; Beloborodov 2017; Ripperda et al. 2022). However, this work suggests that heated plasma formed in the nozzle and at the tearing radius can potentially be another source of high-energy emission. This is especially appealing to explain nonthermal emission in the high-soft and soft-intermediate states of BHXRBs. Those states do not launch any large-scale jets and are thus unlikely to be saturated by magnetic flux (e.g., McKinney et al. 2012), which might be a key ingredient to form a corona where the prime source of dissipation comes from magnetic reconnection (e.g., Ripperda et al. 2022; Liska et al. 2022a). Test-particle methods (e.g., Bacchini et al. 2019) informed by first principles particle-in-cell simulations are an interesting avenue for future research to quantify the contribution of magnetic reconnection and warp-driven shocks to the acceleration of nonthermal particles and corona-like emission.

We thank Michiel van der Klis, Adam Ingram, Sera Markoff, and Ramesh Narayan for insightful discussions. An award of computer time was provided by the Innovative and Novel Computational Impact on Theory and Experiment (INCITE), OLCF Director's Discretionary Allocation, and ASCR Leadership Computing Challenge (ALCC) programs under award PHY129. This research used resources of the Oak Ridge Leadership Computing Facility, which is a DOE Office of Science User Facility supported under Contract DE-AC05-00OR22725. This research used resources of the National Energy Research Scientific Computing Center, a DOE Office of Science User Facility supported by the Office of Science of the U.S. Department of Energy under Contract No. DE-AC02-

05CH11231 using NERSC award ALCC-ERCAP0022634. We acknowledge PRACE for awarding us access to JUWELS Booster at GCS@JSC, Germany. M.L. was supported by the John Harvard Distinguished Science Fellowship, G.M. is supported by a Netherlands Research School for Astronomy (NOVA), Virtual Institute of Accretion (VIA) postdoctoral fellowship, N.K. by an NSF Graduate Research Fellowship, and A.T. by the National Science Foundation grants AST-2206471, AST-2009884,AST-2107839, AST-1815304, OAC-2031997, and AST-1911080.

ORCID iDs

M. T. P. Liska https://orcid.org/0000-0003-4475-9345
N. Kaaz https://orcid.org/0000-0002-5375-8232
G. Musoke https://orcid.org/0000-0003-1984-189X
A. Tchekhovskoy https://orcid.org/0000-0002-9182-2047
O. Porth https://orcid.org/0000-0002-4584-2557

References

Abramowicz, M., Jaroszynski, M., & Sikora, M. 1978, A&A, 63, 221
Abramowicz, M. A., & Kluźniak, W. 2004, in AIP Conf. Ser. 714, X-ray Timing 2003: Rossi and Beyond, ed. P. Kaaret, F. K. Lamb, & J. H. Swank (San Francisco, CA: AIP), 21
Alston, W. N., Parker, M. L., Markevičiūtė, J., et al. 2015, MNRAS, 449, 467
Altamirano, D., Belloni, T., Linares, M., et al. 2011, ApJL, 742, L17
Andalman, Z. L., Liska, M. T. P., Tchekhovskoy, A., Coughlin, E. R., & Stone, N. 2022, MNRAS, 510, 1627
Arcodia, R., Merloni, A., Nandra, K., et al. 2021, Natur, 592, 704
Arzamasskiy, L., & Rafikov, R. R. 2018, ApJ, 854, 84
Bacchini, F., Ripperda, B., Porth, O., & Sironi, L. 2019, ApJS, 240, 40
Balbus, S. A., & Hawley, J. F. 1991, ApJ, 376, 214
Balbus, S. A., & Hawley, J. F. 1998, RvMP, 70, 1
Bardeen, J. M., & Petterson, J. A. 1975, ApJL, 195, L65
Begelman, M. C., & Pringle, J. E. 2007, MNRAS, 375, 1070
Belloni, T., Klein-Wolt, M., Méndez, M., van der Klis, M., & van Paradijs, J. 2000, A&A, 355, 271
Beloborodov, A. M. 2017, ApJ, 850, 141
Chatterjee, K., Liska, M., Tchekhovskoy, A., & Markoff, S. B. 2019, MNRAS, 490, 2200
Chatterjee, K., Younsi, Z., Liska, M., et al. 2020, MNRAS, 499, 362
Clavel, J., Nandra, K., Makino, F., et al. 1992, ApJ, 393, 113
Courant, R., Friedrichs, K., & Lewy, H. 1928, MatAn, 100, 32
Czerny, B., You, B., Kurcz, A., et al. 2016, A&A, 594, A102
Deng, H., & Ogilvie, G. I. 2022, MNRAS, 512, 6078
Deng, H., Ogilvie, G. I., & Mayer, L. 2020, MNRAS, 500, 4248
Dewberry, J. W., Latter, H. N., Ogilvie, G. I., & Fromang, S. 2020a, MNRAS, 497, 435
Dewberry, J. W., Latter, H. N., Ogilvie, G. I., & Fromang, S. 2020b, MNRAS, 497, 451
Dexter, J., & Begelman, M. C. 2019, MNRAS, 483, L17
Doğan, S., & Nixon, C. J. 2020, MNRAS, 495, 1148
Doğan, S., Nixon, C. J., King, A. R., & Pringle, J. E. 2018, MNRAS, 476, 1519
Drewes, N. C., & Nixon, C. J. 2021, ApJ, 922, 243
Fender, R. P., Belloni, T. M., & Gallo, E. 2004, MNRAS, 355, 1105
Fragile, P. C., & Anninos, P. 2005, ApJ, 623, 347
Fragile, P. C., & Blaes, O. M. 2008, ApJ, 687, 757
Fragile, P. C., Blaes, O. M., Anninos, P., & Salmonson, J. D. 2007, ApJ, 668, 417
Fragile, P. C., Etheridge, S. M., Anninos, P., Mishra, B., & Kluzniak, W. 2018, ApJ, 857, 1
Gardiner, T. A., & Stone, J. M. 2005, JCoPh, 205, 509
Gierlinski, M., & Done, C. 2004, MNRAS, 349, L7
Gierlinski, M., & Done, C. 2006, MNRAS, 371, L16
Gierlinski, M., Middleton, M., Ward, M., & Done, C. 2008, arXiv:0807.1899
Giustini, M., Miniutti, G., & Saxton, R. D. 2020, A&A, 636, L2
Hankla, A. M., Scepi, N., & Dexter, J. 2022, MNRAS, 515, 775
Hawley, J. F., & Krolik, J. H. 2018, ApJ, 866, 5
Ingram, A., Done, C., & Fragile, P. C. 2009, MNRAS, 397, L101
Ingram, A., & van der Klis, M. 2014, MNRAS, 446, 3516
Ingram, A., van der Klis, M., Middleton, M., et al. 2016, MNRAS, 461, 1967
Ingram, A. R., & Motta, S. E. 2019, NewAR, 85, 101524
Jiang, Y.-F., Blaes, O., Stone, J. M., & Davis, S. W. 2019, ApJ, 885, 144
Kaaz, N., Liska, M. T. P., Jacquemin-Ide, J., et al. 2022, arXiv:2210.10053
Kara, E., Steiner, J. F., Fabian, A. C., et al. 2019, Natur, 565, 198
Kato, S. 2004, PASJ, 56, 905
King, A. 2020, MNRAS, 493, L120
Kitaki, T., Mineshige, S., Ohsuga, K., & Kawashima, T. 2021, arXiv:2101.11028
Kluzniak, W., & Abramowicz, M. A. 2002, arXiv:astro-ph/0203314
Kochanek, C. S. 1994, ApJ, 422, 508
Kulkarni, A. K., Penna, R. F., Shcherbakov, R. V., et al. 2011, MNRAS, 414, 1183
Lawrence, A. 2018, NatAs, 2, 102
Lense, J., & Thirring, H. 1918, PhyZ, 19, 156
Levermore, C. D. 1984, JQSRT, 31, 149
Lightman, A. P., & Eardley, D. M. 1974, ApJL, 187, L1
Lin, D., Webb, N. A., & Barret, D. 2014, ApJ, 780, 39
Liska, M., Hesp, C., Tchekhovskoy, A., et al. 2018, MNRAS, 474, L81
Liska, M., Hesp, C., Tchekhovskoy, A., et al. 2019a, arXiv:1901.05970
Liska, M., Hesp, C., Tchekhovskoy, A., et al. 2021, MNRAS, 507, 983
Liska, M., Tchekhovskoy, A., Ingram, A., & van der Klis, M. 2019b, MNRAS, 487, 550
Liska, M. T. P., Musoke, G., Tchekhovskoy, A., Porth, O., & Beloborodov, A. M. 2022a, ApJL, 935, L1
Liska, M. T. P., Chatterjee, K., Issa, D., et al. 2022b, ApJS, 263, 26
MacLeod, C. L., Ross, N. P., Lawrence, A., et al. 2016, MNRAS, 457, 389
McKinney, J. C., Chluba, J., Wielgus, M., Narayan, R., & Sadowski, A. 2017, MNRAS, 467, 2241
McKinney, J. C., Tchekhovskoy, A., & Blandford, R. D. 2012, MNRAS, 423, 3083
McKinney, J. C., Tchekhovskoy, A., & Blandford, R. D. 2013, Sci, 339, 49
Meier, D. L. 2012, BH Astrophysics: The Engine Paradigm (Berlin: Springer)
Miniutti, G., Giustini, M., Arcodia, R., et al. 2022, arXiv:2207.07511
Miniutti, G., Saxton, R. D., Giustini, M., et al. 2019, Natur, 573, 381
Mishra, B., Fragile, P. C., Anderson, J., et al. 2022, ApJ, 939, 31
Mishra, B., Fragile, P. C., Johnson, L. C., & Kluźniak, W. 2016, MNRAS, 463, 3437
Mishra, B., Kluźniak, W., & Fragile, P. C. 2020, MNRAS, 497, 1066
Musoke, G., Liska, M., Porth, O., van der Klis, M., & Ingram, A. 2023, MNRAS, 518, 1656
Narayan, R., Igumenshchev, I. V., & Abramowicz, M. A. 2003, PASJ, 55, L69
Narayan, R., & Yi, I. 1994, ApJL, 428, L13
Nealon, R., Price, D. J., & Nixon, C. J. 2015, MNRAS, 448, 1526
Neilsen, J., Remillard, R. A., & Lee, J. C. 2011, ApJ, 737, 69
Nelson, R. P., & Papaloizou, J. C. B. 2000, MNRAS, 315, 570
Newman, W. I., & Hamlin, N. D. 2014, SJSC, 36, B661
Nixon, C., King, A., Price, D., & Frank, J. 2012a, ApJL, 757, L24
Nixon, C., & Salvesen, G. 2013, MNRAS, 437, 3994
Nixon, C. J., & King, A. R. 2012, MNRAS, 421, 1201
Nixon, C. J., King, A. R., & Price, D. J. 2012b, MNRAS, 422, 2547
Noble, S. C., Gammie, C. F., McKinney, J. C., & Del Zanna, L. 2006, ApJ, 641, 626
Noble, S. C., Krolik, J. H., & Hawley, J. F. 2009, ApJ, 692, 411
Novikov, I. D., & Thorne, K. S. 1973, BHs (Les Astres Occlus), ed. C. Dewitt & B. S. Dewitt (New York: Gordon and Breach), 343
Ogilvie, G. I. 1999, MNRAS, 304, 557
Ogilvie, G. I. 2018, MNRAS, 477, 1744
Ogilvie, G. I. 2022, MNRAS, 513, 1701
Ogilvie, G. I., & Dubus, G. 2001, MNRAS, 320, 485
Ogilvie, G. I., & Latter, H. N. 2013, MNRAS, 433, 2420
Paardekooper, S.-J., & Ogilvie, G. I. 2018, MNRAS, 483, 3738
Papaloizou, J. C. B., & Lin, D. N. C. 1995, ARA&A, 33, 505
Papaloizou, J. C. B., & Pringle, J. E. 1983, MNRAS, 202, 1181
Piran, T., Sądowski, A., & Tchekhovskoy, A. 2015, MNRAS, 453, 157
Porth, O., Chatterjee, K., Narayan, R., et al. 2019, ApJS, 243, 26
Pringle, J. E. 1997, MNRAS, 292, 136
Raj, A., & Nixon, C. J. 2021, ApJ, 909, 82
Raj, A., Nixon, C. J., & Dogan, S. 2021, ApJ, 909, 81
Rees, M. J. 1988, Natur, 333, 523
Remillard, R. A., & McClintock, J. E. 2006, ARA&A, 44, 49
Ressler, S. M., Tchekhovskoy, A., Quataert, E., Chandra, M., & Gammie, C. F. 2015, MNRAS, 454, 1848
Ressler, S. M., Tchekhovskoy, A., Quataert, E., & Gammie, C. F. 2017, MNRAS, 467, 3604
Rezzolla, L., Yoshida, S., & Zanotti, O. 2003, MNRAS, 344, 978

Ripperda, B., Liska, M., Chatterjee, K., et al. 2022, ApJL, 924, L32
Rowan, M. E., Sironi, L., & Narayan, R. 2017, ApJ, 850, 29
Russell, D. M., Casella, P., Kalemci, E., et al. 2020, MNRAS, 495, 182
Sadowski, A. 2011, arXiv:1108.0396
Sądowski, A. 2016, MNRAS, 459, 4397
Sądowski, A., & Narayan, R. 2015, MNRAS, 454, 2372
Shakura, N. I., & Sunyaev, R. A. 1973, A&A, 24, 337
Shakura, N. I., & Sunyaev, R. A. 1976, MNRAS, 175, 613
Shiokawa, H., Dolence, J. C., Gammie, C. F., & Noble, S. C. 2012, ApJ, 744, 187
Sironi, L., & Spitkovsky, A. 2014, ApJL, 783, L21
Sądowski, A., Narayan, R., Tchekhovskoy, A., & Zhu, Y. 2013, MNRAS, 429, 3533
Smith, K. L., Mushotzky, R. F., Boyd, P. T., & Wagoner, R. V. 2018, ApJL, 860, L10
Sniegowska, M., Czerny, B., Bon, E., & Bon, N. 2020, A&A, 641, A167
Sobolewska, M. A., & Życki, P. T. 2006, MNRAS, 370, 405
Sorathia, K. A., Krolik, J. H., & Hawley, J. F. 2013, ApJ, 768, 133
Stella, L., & Vietri, M. 1998, ApJL, 492, L59
Stepney, S. 1983, MNRAS, 202, 467
Tchekhovskoy, A., Narayan, R., & McKinney, J. C. 2011, MNRAS, 418, L79
Teixeira, D. M., Fragile, P. C., Zhuravlev, V. V., & Ivanov, P. B. 2014, ApJ, 796, 103
Uttley, P., Cackett, E. M., Fabian, A. C., Kara, E., & Wilkins, D. R. 2014, A&ARv, 22, 72
Wagoner, R. V., & Tandon, C. R. 2021, ApJ, 920, 114
Weng, S.-S., Wang, T.-T., Cai, J.-P., Yuan, Q.-R., & Gu, W.-M. 2018, ApJ, 865, 19
White, C. J., Quataert, E., & Blaes, O. 2019, ApJ, 878, 51
White, C. J., Stone, J. M., & Gammie, C. F. 2016, ApJS, 225, 22
Wijers, R. A. M. J., & Pringle, J. E. 1999, MNRAS, 308, 207
Yang, Q., Wu, X.-B., Fan, X., et al. 2018, ApJ, 862, 109
Zhang, P., Zhang, P.-f., Yan, J.-z., Fan, Y.-z., & Liu, Q.-z. 2017, ApJ, 849, 9
Zhang, S. N., Cui, W., & Chen, W. 1997, ApJL, 482, L155
Zhu, Y., Davis, S. W., Narayan, R., et al. 2012, MNRAS, 424, 2504